PHYSICAL REVIEW B **112**, 134410 (2025)

Relaxation pathways and emergence of domains in square artificial spin ice

Matteo Menniti[1] Naëmi Leo[1,2,*] Pedro Villalba-González[1,3] Matteo Pancaldi[4] and Paolo Vavassori[1,5,†]
[1]CIC nanoGUNE BRTA, 20018 Donostia–San Sebastián, Spain
[2]Department of Physics, School of Science, Loughborough University, LE11 3TU Loughborough, United Kingdom
[3]Department of Physics and Astronomy, University of British Columbia, Vancouver, British Columbia V6T 1Z1, Canada
[4]Elettra-Sincrotrone Trieste S.C.p.A., 34149 Basovizza, Trieste, Italy
[5]IKERBASQUE, Basque Foundation for Science, E-48009 Bilbao, Spain

(Received 29 May 2025; revised 30 August 2025; accepted 3 September 2025; published 7 October 2025)

Multidomain states of square artificial spin ice show a range of different morphologies ranging from simple stripelike domains to more organically shaped coral domains. To model the relevant dynamics leading to the emergence of such diverse domain structures, simplified descriptions of the switching behavior of individual nanomagnets are necessary. In this work, we employ kinetic Monte Carlo simulations of the demagnetization of square artificial spin ice toward its ground state and compare how the choice of transition barriers affect the emergence of mesoscale domains. We find that the commonly used mean-field barrier model (informed by equilibrium energetics only) results in propagation of ground-state string avalanches. In contrast, taking into account chiral barrier splitting enabled by state-dependent local torques supports the emergence of complex-shaped coral domains and their successful relaxation towards the ground state in later relaxation stages. Our results highlight that intrinsic contributions to switching barriers, in addition to the effect of extrinsic defects often attributed to nanofabrication irregularities, can subtly shift favored transition pathways and result in different emergent mesoscale features. Future kinetic Monte Carlo models that describe the evolution of artificial spin systems should thus account for these effects.

DOI: 10.1103/9mlg-ckxl

I. INTRODUCTION

Artificial spin ices (ASI) are metamaterials in which networks of interacting nanomagnets [1–4] are used to study phenomena such as phase transitions and emergent correlations in geometrically frustrated spin systems [5–9] or using their self-organizing behavior for low-power unconventional computing [10–14]. A key question common to all these effects is how mutual interactions between the basic constituents (i.e., nanomagnets) impact the evolution of macroscopic variables, the emergence of mesoscale domains [15,16], and the successful relaxation to the ground state of the system [1,17–19]. Over the years, different mechanisms have been implemented to excite artificial spin systems, ranging from oscillating or rotating magnetic fields [20–24], thermalization during sample growth [15,25–27], thermal annealing after growth [28–30], as well as thermalization at constant temperature using superparamagnetic nanomagnets [17,31–37].

A well-studied specific lattice geometry is the square artificial spin ice (s-ASI), where four nanomagnets are arranged on crosslike vertices, as shown in Fig. 1(a). The s-ASI has a well-defined antiferromagnetic ground state made up of a tiling of so-called T_1 vertices [Fig. 1(b)] [1,62], which makes it attractive for comparative studies tracking its relaxation via successive moment reversals lowering the net interaction energy of the system [12,18].

A particularly intriguing observation in relaxation studies relates to the emergent mesoscale structures imaged by magnetic microscopy, which can come in two distinct flavors: On the one hand, relaxation driven by avalanches of T_1 strings results in *diagonal stripelike domains* that clearly mirror the underlying energy hierarchy of the system [17,23,31,35,38]. On the other hand, organically shaped *coral domains*—delimited by domain boundaries oriented along *any* lattice directions (and thus not necessarily coinciding with the diagonal string propagation) [15,26–30]—are usually attributed to extrinsic site-specific disorder originating from nanofabrication defects [22,38–41].

Supplementing experimental observations, Monte Carlo simulations based on simplified assumptions are often used to explain key features in the evolution of artificial spin systems [12,38,42–44]. Recently, we showed that chiral barrier splitting enabled by state-specific local torques has been overlooked so far in the description of switching behavior in s-ASI [45,46]. Taking local fields into account, the switching barriers are significantly reduced in strongly interacting s-ASI, leading to faster relaxation as well as modifying favored relaxation pathways.

In this work, we expand on these findings on the demagnetization of s-ASI using kinetic Monte Carlo (kMC) simulations, comparing a model based on purely equilibrium energy considerations (mean-field model) with a model

---

[*] Contact author: n.leo@lboro.ac.uk
[†] Contact author: p.vavassori@nanogune.eu

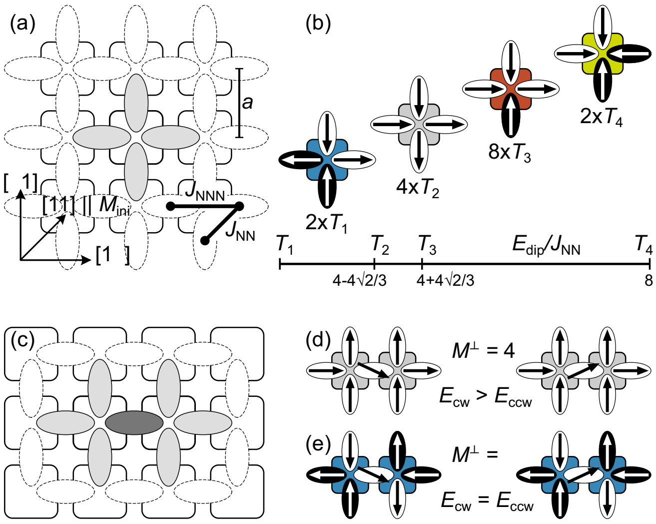

FIG. 1. Square artificial spin ice. (a) Geometry of tiled four-moment vertices with lattice periodicity a and nearest- and next-nearest neighbor interactions J_{NN}^{dip} and J_{NNN}^{dip}. (b) Energy hierarchy and multiplicity of single-vertex configurations T_i $(i = 1 \cdots 4)$. (c) The double-vertex environment (light gray) acting on the central island (dark gray) determines the energy barrier for moment switching. [(d) and (e)] For reversal via coherent rotation a perpendicular magnetization $M^{\perp} \neq 0$ exerted by the environment can lift the degeneracy for clockwise and counterclockwise reversal energy barriers.

that takes into account the local contributions to the kinetic switching barriers. We find that—even in the absence of disorder—the modifications due to chiral barrier splitting can lead to the formation of coral domains and identify the relevant relaxation pathways that favor the formation of complex-shaped domains as well as their final consolidation towards a global ground state. Our results demonstrate how the influence of intrinsic interactions, in addition to extrinsic disorder, can lead to the emergence of complex mesoscale domain patterns, an effect which should be considered for future modeling of relaxation of artificial spin systems.

II. BACKGROUND

Here we consider the s-ASI lattice with periodic boundary conditions, which is formed by $n \times n$ four-moment vertices (i.e., in total $2n^2$ moments), as shown in Fig. 1(a). Due to rapid interaction dropoff, it is sufficient to consider interactions between nearest and next-nearest neighbors [27,38,42,46]. Within the point-dipole approximation, interaction strengths J_{NN}^{dip} and J_{NNN}^{dip} depend on the lattice periodicity a and magnetic moment m only, with μ_0 being the magnetic permeability:

$$J_{NN}^{\text{dip}} = \tfrac{3}{\sqrt{2}} \frac{\mu_0}{2\pi} \frac{m^2}{a^3} \quad \text{and} \tag{1}$$

$$J_{NNN}^{\text{dip}} = \frac{\mu_0}{2\pi} \frac{m^2}{a^3} = \frac{\sqrt{2}}{3} J_{NN}^{\text{dip}} \approx 0.47 J_{NN}^{\text{dip}}\,. \tag{2}$$

The 16 possible states of a four-moment vertex define an energy hierarchy with four distinct cases, Fig. 1(b). The two lowest-energy states are ground-state T_1 configurations (blue) and T_2 vertices (gray) that can be initialized by a diagonal saturating magnetic field. The T_1 and T_2 configurations obey the so-called two-in-two-out "ice rule" [1], whereas T_3 (red) and T_4 (yellow) are high-energy configurations associated with magnetic charges. T_4 configurations are especially unfavorable and rarely occur in experiments or simulations [15,47].

In this work, we consider the thermal demagnetization from a field-set initial state of T_2 vertices to a low-energy configuration dominated by T_1 vertices [23,31,38]. Full demagnetization requires every other moment to flip, and thus at least n^2 spin flips to reach the ground state. However, any transition from a T_2 to a T_1 state requires the excitation of higher-energy T_3 vertices, as mutual interactions restrict the relaxation pathways [12,18].

To model the time-dependent demagnetization, the transition rates $\nu(\Delta E, T)$ for thermally activated moment reversals can be expressed by the Arrhenius law:

$$\nu(\Delta E, T) = \nu_0 \exp\left(-\frac{\Delta E}{k_B T}\right). \tag{3}$$

Here ΔE is the energy barrier to be overcome, T is the absolute temperature, and k_B the Boltzmann constant [48,49]. The prefactor ν_0 is a rate typically in the order of 10^8–10^{12}s^{-1} and depends on the size and temperature of the nanomagnet [48,50,51]. Here we assume that ν_0 is state independent or at least varies much less than the exponential dependence with the barrier energy [52,53].

As shown in Fig. 1(c), a moment surrounded by six closest neighbors forms a double-vertex configuration that determines the energy contribution to the switching barrier ΔE. For s-ASI in the limit of quasicoherent moment reversal, ΔE can be decomposed into three contributions [45,46].

First, the single-particle barrier ΔE_{sb} is associated with the shape anisotropy of a noninteracting magnetic nanoisland [10,54–56]. In this work, we use τ_{sb} as a natural timescale of the evolution:

$$\tau_{\text{sb}}^{-1} = \nu(\Delta E_{\text{sb}}, T). \tag{4}$$

Second, the single-particle barrier is modified by the pairwise interactions and favors transitions to configurations of lower dipolar energy. Using the energy difference $\Delta E_{i\to f}^{\text{dip}} = E_f^{\text{dip}} - E_i^{\text{dip}}$ between final and initial static moment configurations, the "mean-field" (MF) [11,12,18,45,46] switching rate is given by

$$\nu_i^{\text{MF}} = 2\nu_0 \exp\left(-\frac{\Delta E_{\text{sb}} + \frac{1}{2}\Delta E_{i\to f}^{\text{dip}}}{k_B T}\right. . \tag{5}$$

Third, as shown in Figs. 1(d) and 1(e), the four nearest-neighbor moments can exert a torque via a local perpendicular net magnetization $M_i^{\perp}$ acting on the switching moment. If $M_i^{\perp} \neq 0$, then the energy barriers for clockwise (↻) and counterclockwise (↺) switching differ [45,46]:

$$\Delta E_{i\to f,\circlearrowright/\circlearrowleft} = \Delta E_{\text{sb}} + \frac{1}{2}\Delta E_{i\to f}^{\text{dip}} \pm \frac{M_i^{\perp}}{3} J_{NN}^{\text{dip}}. \tag{6}$$

This chiral barrier splitting is present for a large fraction of magnetic configurations [46], including the fully magnetized background [Fig. 1(d)] where, with $M_i^{\perp} = +4$, a counterclockwise reversal is favorable over a clockwise moment rotation. In contrast, barrier splitting is absent for example for the ground-state configuration with $M_i^{\perp} = 0$ [Fig. 1(e)].

Due to the exponential behavior of the Arrhenius law in Eq. (3), even a small reduction of the energy barrier significantly increases the switching rate through the favored (clockwise or counterclockwise) reversal channel. In the following we denote the increased net relaxation rate as “chiral-split barrier model” or CB:

$$\nu_i^{\mathrm{CB}} = \nu_i^{\circlearrowright} + \nu_i^{\circlearrowleft} = \nu_i^{\mathrm{MF}} \cosh\left(M_i^{\perp} \frac{J_{NN}^{\mathrm{dip}}}{3k_B T} \right). \tag{7}$$

III. METHODS

We performed kMC simulations [57–59] of the demagnetization of s-ASI, using a custom-written `pyt on` kMC code [60,61], comparing the relaxation behavior of mean-field and chiral-split barrier models [45,46]. Periodic boundary conditions ensure that all moments have the same double-vertex environment, emulating a larger network without edge effects. In particular, we assume a perfect system with equal moments, that is, we do not take into account the effect of defects or site-specific variations in switching barriers. The purely configuration-dependent probabilities for successive spin flips are calculated from the current state and using a lookup table for the double-vertex transition rates calculated from Eq. (5) and Eq. (7), respectively. For each kMC step, a single moment is flipped after being randomly selected from the weighted transition probabilities, and, together with a random time update (again, based on the most likely transition rates), the system is updated [57–59,61].

The single-particle switching barrier $E_{\mathrm{sb}} = 1.327\,\mathrm{eV}$ and moment $m = 3.285\times10^6\ \mu_B$ correspond to values for a stadium-shaped permalloy island with length, width, and height of 150 nm × 100 nm × 3 nm and a saturation magnetization of 790 kA/m. As shown in previous works [45,46] such a magnetic nanoisland reverses via quasiuniform modes and thus is an appropriate choice for our study [24,32].

The lattice periodicity a, and thus the strength of J_{NN}^{dip} in Eq. (1), has been varied between values of 150 and 500 nm. The resulting Néel temperatures, $T_N(a) = 1.7 J_{NN}^{\mathrm{dip}}(a)$ [42,62], is always above the fixed simulation temperature of $T = 300\,\mathrm{K}$ with ratios T_N/T ranging from 1.3 (i.e., close to the transition to the paramagnetic phase) to ≈30 (i.e., T 0) (see Fig. 6 in the Appendix).

We chose to simulate a s-ASI with a system size of 50×50 vertices ($2n^2 = 5000$ moments), compromising between statistics and computational resources (see Fig. 7 in the Appendix). The initial configuration is fully magnetized with $M_{\mathrm{ini}} \parallel [11]$ parallel to the diagonal [11] direction [see Fig. 1(a)], and the system is given $n^3 = 125\times10^3$ steps to relax. For each value of a and the barrier model, at least 20 kMC runs have been executed to ensure meaningful statistics.

IV. RESULTS

To compare the relaxation timescales, Fig. 2 shows the mean time $\langle t(M^{[11]} = 75\%)\rangle_{\mathrm{runs}}$, normalized to τ_{sb}. For the mean-field model (blue squares) we find that with strong interactions J_{NN}^{dip} (respectively, lattice periodicities a 240 nm) the speed of initial demagnetization are slowed down even beyond the single-moment switching time. This is in contrast to the chiral-split barrier model (red circles) for which the demagnetization evolves significantly faster but slows down with increasing lattice periodicity a and approaches the mean-field model. This convergence arises from the fact that the interaction strength $J_{NN}^{\mathrm{dip}} \propto a^{-3}$ rapidly decreases and the transition barriers are dominated by E_{sb} only [alternatively, $T_N(a)$ T, see Figs. 6 and 8 in the the Appendix]. For small a 240 nm the relaxation in both models slows down at different rates (due to reasons discussed in the next section), with the relaxation timescales for mean-field barrier model exceeding that of the single-particle relaxation timescale given by τ_{sb}.

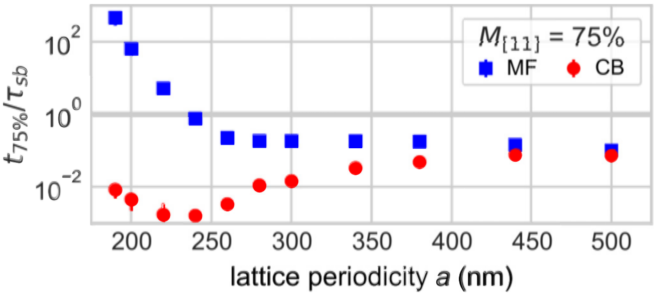

FIG. 2. Average time at which $M_{[11]} = 75\%$ for the mean-field barrier model (blue squares) and the chiral-split barrier model (red circles). Both models approach each other at large lattice periodicities a. For strong interactions (small lattice periodicity a), the mean-field model shows slower evolution compared to the chiral-barrier model, as the latter generally features faster kinetics due to the reduction of switching barriers. For periodicities a 240 nm both models show an apparent slowdown. For the mean-field model, this slowdown is even beyond the single-particle relaxation timescale τ_{sb} due to string propagation being the only significant relaxation pathway. For the split-barrier model, the slowdown originates from the effect of kinetic blocking via subsequent creation and annihilation of T_3 vertices.

Figure 3 shows kMC results of the demagnetization process in s-ASI with lattice periodicities $a = 200$, 240 and 280 nm (from left to right), comparing the behavior of the mean-field barrier model [Figs. 3(a)–3(c)] to that of the chiral-split barrier model [Figs. 3(d)–3(f)]. The black lines track the net magnetization $M_{[11]}(t/\tau_{\mathrm{sb}})$ for each kMC run (left scale) with the time t normalized to the switching timescale τ_{sb} of a noninteracting moment defined in Eq. (4).

The magnetization $M^{[11]}(t)$ decreases on an exponential timescale to a value of around 25% of the initial moment, after which the relaxation slows down considerably. Especially in the case of the chiral-split barrier model, the evolution can continue to a value of $M^{[11]}(t) \approx 0$, which, however, does *not* imply that a fully relaxed T_1 ground state has been reached. For the mean-field model, full demagnetization is less often observed due to a limited simulation time window, as well as kinetic blocking of effective relaxation in later stages (discussed in Sec. IV C).

It is instructive to also consider the vertex populations of T_3 (red). For lattice periodicities a 250 nm the initial demagnetization from $M^{[11]} = 100\%$ to 50% is accompanied by a small stable population of T_3 vertices (0.5%, i.e., corresponding to at most 14 vertices in our system), indicating correlated demagnetization. At higher values of a, respectively weaker interactions, the T_3 population peaks at a time where $M^{[11]} \approx 75\%$, indicating more randomized

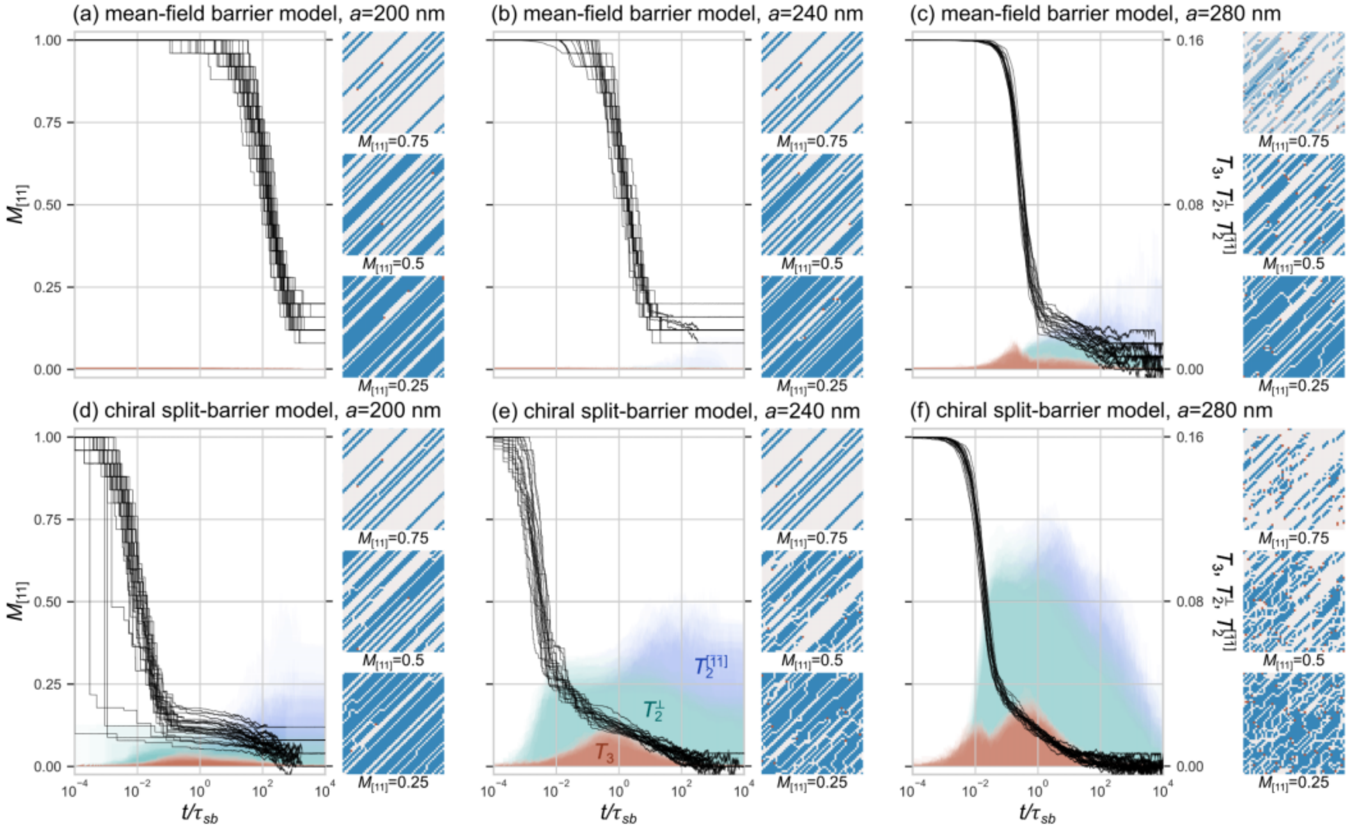

FIG. 3. Demagnetization behavior for different lattice periodicities a for [(a)–(c)] the mean-field barrier model and [(d)–(f)] the chiral-split barrier model. Black lines show the time evolution of the net magnetization $M^{[11]}(t)$ of different kMC runs (left-handed scale from 0 to 1). Shaded areas (right-handed scale from 0 to 0.16) denote the population of T_3 vertices (red, in forefront) and T_2 vertices that do not align with the initial [11] direction, separated into rotated $T_2^{\perp}$ (cyan, from zero) and reversed $T_2^{[\bar{1}\bar{1}]}$ (blue, stacked on $T_2^{\perp}$ population). Insets on the right show representative spatial configurations of vertices at times where the net magnetization is at 75%, 50% and 25% of its initial value. Vertex color coding is equivalent to Fig. 1(a).

demagnetization, as shown in Figs. 3(c) and 3(f) as well as Fig. 8. A later peak in T_3 vertices around $M_{[11]} \approx 10\%$ is associated with dynamics confined to ground-state domain boundaries, with further details discussed in Sec. IV D.

Further insights into the relaxation behavior can be obtained from representative real-space snapshots of the magnetic configuration at $M^{[11]} = 75\%$, 50% and 25%, shown in the three panels on the right side of each graph, with vertex color coding according to Fig. 1(b). For the mean-field model, Figs. 3(a)–3(c), the snapshots are dominated by diagonal lines of T_1 vertices (blue), related to the avalanche-like propagation of T_1 "strings" through the fully magnetized background (gray) [23,35,38,63]. For the chiral-split barrier model, Figs. 3(d)–3(f), the picture is more diverse, with more T_3 vertices present and T_1 strings broken up by sideways interruptions, and at $M^{[11]} = 25\%$ (lower panels) indications for the emergence of coral-shaped ground-state domains [15,28,29].

A. Initial demagnetization: Pathways

To understand the preferred switching pathways and relaxation regimes in Fig. 4 we compare the relative transition rates for the initial demagnetization steps of the s-ASI. Figure 4(a) shows the spin configuration after a first spin flip on a random site within the magnetized T_2 background, which creates a pair of higher-energy T_3 vertices. Possible next transitions are labeled with letters A to D. Transition A creates a ground-state T_1 vertex along the [11] diagonal. In contrast, transition D would create a T_4 vertex and thus is unlikely to occur (dimmed gray label). The imbalance between transitions A and D drives the distinct demagnetization parallel with M_{ini} and the emergence of T_1 strings [23,35,38]. Further possible transitions are the creation of an independent T_3 pair (transition B, not labeled explicitly), a flip-back to the original saturated T_2 state (transition B*), or the sideways separation of the T_3 pair (transition C).

The probabilities p_i for possible transitions $i = (A, B, B^*, C, D)$ can be calculated according to

$$p_i^{\text{model}} = \frac{N_i \nu_i^{\text{model}}}{\sum_j N_j \nu_j^{\text{model}}}. \tag{8}$$

The transition rates $\nu_i^{\text{model}}(a, T)$ for the mean-field (chiral-split) barrier model can be calculated from Eq. (5) [Eq. (7)], using the value of $J_{NN}^{\text{dip}} \propto a^{-3}$ according to Eq. (1). The corresponding energy differences $E_{i\ f}^{\text{dip}}$, perpendicular magnetization $M_i^{\perp}$ and number of possible sites N_i after the first spin flips are listed in Table I.

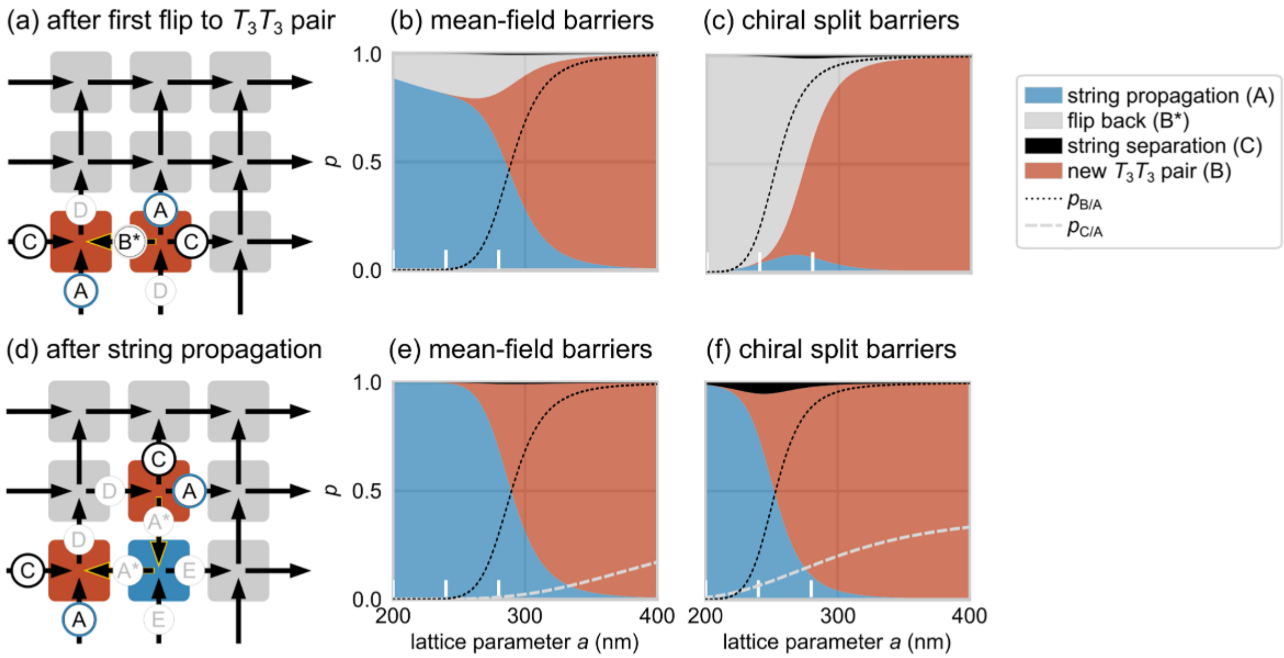

FIG. 4. Initial demagnetization steps. (a) Spin configuration after a first spin flip creating a T_3 pair. Distinct transitions are labeled with letters, and unmarked moments are of transition type B (T_2T_2 T_3T_3, see Table I). Transitions which are highly unlikely to occur are marked in light gray (e.g., transition D). [(b) and (c)] Transition probabilities p_i in dependence of the lattice periodicity a for (b) mean-field barrier energies and (c) when taking into account additional chiral splitting of the barriers. The probability $p_{B/A}$ (black dotted line) demarks the transition between demagnetization dominated via string propagation (transition A, blue) and creation of new T_3 pairs (B, red). Flip back transitions that restore the initial fully magnetized T_2 state can be highly probable (B*, gray), and, in the case of the split-barrier model, are favored for strong interactions [i.e., smaller a in (c)]. White markers indicate the lattice periodicities a shown in Fig. 3. (d) Spin configuration and labeled transition after the formation of a first T_1 vertex (protostring), which is a stable emerging magnetic texture. [(e) and (f)] Comparison of model-dependent transition probabilities. The probability $p_{C/A}$ (dashed gray line) indicates the ratio of string separation (transition C) over string propagation events (transition A). String separation events result in $T_2^{\perp}$ vertices important for the formation of coral-shaped domain states, and are more likely to occur for the split-barrier model.

Figures 4(b) and 4(c) show stacked plots of the relative transition probabilities in dependence of the lattice constant a for the mean-field and chiral-split barrier model, respectively. One major difference between both models is the backflip probability (transitions B*) after creation of a T_3 pair (gray area). In the case of the chiral-split barrier model and for strong interactions $J_{NN}^{\mathrm{dip}} \propto a^{-3}$ transition B* is the preferred relaxation pathway, due to the reduction of the switching barrier enabled by high local torques. In a defect-free system (as is the case in our simulations), the constant creation and annihilation of T_3 pairs (transitions B*) creates a situation of "kinetic blocking," which delays the onset of the demagnetization via T_1 string propagation (see Fig. 2).

Apart from the peculiarity of back-flips boosted by chiral barrier splitting, the two main pathways toward efficient demagnetization are either the string propagation (transition A, blue) or the creation of new T_3 pairs (transition B, red). The former transition is energetically preferred as it creates a ground-state T_1 vertex, whereas the probability for the latter is enhanced by the $2n^2$–7 sites in which the transition can take place (see Table I). The relative probability $p_{B/A}$ of these two transitions can be calculated as

$$p_{B/A}^{\mathrm{model}} = \frac{N_B \nu_B^{\mathrm{model}}}{N_A \nu_A^{\mathrm{model}} + N_B \nu_B^{\mathrm{model}}}, \quad (9)$$

and is shown as dotted black line in Figs. 4(b) and 4(c). This line demarks the range of lattice periodicity a where one relaxation pathway is favored over the other. In contrast, for the chiral-split barrier model, demagnetization via T_3 pair formation becomes favored over string propagation at smaller values of a, compared to the mean-field barrier model.

Once a T_1 string is nucleated, Fig. 4(d), the relative importance of the relaxation pathways shifts dramatically, see Figs. 4(e) and 4(f). In particular, the T_1 vertices enjoy remarkable stability, with back-flip A* or transitions D and E extremely unlikely. For the mean-field barrier model and low values of a 240 nm, string propagation remains the *only* available relaxation pathway. Due to the way the kMC simulations are implemented [60,61], the update time on each step is dominated by the much larger energy barrier needed to form a new T_3 pair on the approximately $\approx 2n^2 - m$ sites (with m being the string length), leading to the exceptional slowdown in Fig. 2.

In general, the main evolution of the T_1 string occurs via diagonal T_3 propagation creating more T_1 vertices (transition A, blue) or the sideways separation of T_3 vertices (C, black), creating a $T_2^{\perp}$ vertex whose moments points perpendicular to M_{ini}. In Figs. 4(e) and 4(f) the relative probability

$$p_{C/A}^{\mathrm{model}} = \frac{N_C \nu_C^{\mathrm{model}}}{N_A \nu_A^{\mathrm{model}} + N_C \nu_C^{\mathrm{model}}}, \quad (10)$$

TABLE I. Transition barriers for Figs. 4 and 5, labeled A to L. For each panel, possible transitions are sorted by increasing mean-field barrier $E^{\mathrm{dip}}_{i\quad f}$, respectively, decreasing transition rate. The barrier energies are both given in multiples of J^{dip}_{NN} and J^{dip}_{NNN} (left), as well as approximate multiples of J^{dip}_{NN} (right). The value of $M_i^{\perp}$ indicates whether the switching macrospin is subject to a torque by its magnetic neighborhood, a condition that enables chiral barrier splitting. The last column denotes the number of possible sites N_i for each spin flip shown in Figs. 4(a) and 4(d), which are necessary to calculate initial transition probabilities.

	Transition	$E^{\mathrm{dip}}_{i\quad f}$		$M_i^{\perp}$	N_i
Fig. 4(a): Transitions after initial T_3T_3 pair					
A	$T_3T_2 \qquad T_1T_3$	$-4J^{\mathrm{dip}}_{NN}+4J^{\mathrm{dip}}_{NNN}$	-2.11	±2	2
B*	$T_2T_2 \leftarrow T_3T_3$	$-4J^{\mathrm{dip}}_{NNN}$	-1.89	±2	1
C	$T_3T_2 \qquad T_2^{\perp}T_3$	0	0	±4	2
B	$T_2T_2 \qquad T_3T_3$	$+4J^{\mathrm{dip}}_{NNN}$	$+1.89$	±4	$2n^2-7$
D	$T_3T_2 \qquad T_4T_3$	$+4J^{\mathrm{dip}}_{NN}+4J^{\mathrm{dip}}_{NNN}$	$+5.89$	±2	2
Fig. 4(b): Transitions after string formation					
A	$T_3T_2 \qquad T_1T_3$	$-4J^{\mathrm{dip}}_{NN}+4J^{\mathrm{dip}}_{NNN}$	-2.11	±2	2
C	$T_3T_2 \qquad T_2^{\perp}T_3$	0	0	±4	2
B	$T_2T_2 \qquad T_3T_3$	$+4J^{\mathrm{dip}}_{NNN}$	$+1.89$	±2	$2n^2-10$
A*	$T_3T_2 \leftarrow T_1T_3$	$+4J^{\mathrm{dip}}_{NN}-4J^{\mathrm{dip}}_{NNN}$	$+2.11$	±2	2
E	$T_1T_2 \qquad T_3T_3$	$+4J^{\mathrm{dip}}_{NN}$	$+4$	±2	2
D	$T_2T_3 \qquad T_4T_3$	$+4J^{\mathrm{dip}}_{NN}+4J^{\mathrm{dip}}_{NNN}$	$+5.89$	±2	2
Fig. 5: Transitions at domain boundaries					
F*	$T_1T_2 \leftarrow T_3T_3$	$-4J^{\mathrm{dip}}_{NN}$	-4	±2	
A	$T_3T_2 \qquad T_1T_3$	$-4J^{\mathrm{dip}}_{NN}+4J^{\mathrm{dip}}_{NNN}$	-2.11	±2	
G*	$T_3T_3 \qquad T_2T_2$	$-4J^{\mathrm{dip}}_{NNN}$	-1.89	0	
H	$T_3T_1 \leftrightarrow T_1T_3$	0	0	0	
J	$T_2T_3 \leftrightarrow T_3T_2$	0	0	0	
G	$T_3T_3 \leftarrow T_2T_2$	$+4J^{\mathrm{dip}}_{NNN}$	$+1.89$	0	
A*	$T_3T_2 \leftarrow T_1T_3$	$+4J^{\mathrm{dip}}_{NN}-4J^{\mathrm{dip}}_{NNN}$	$+2.11$	±2	
F	$T_1T_2 \qquad T_3T_3$	$+4J^{\mathrm{dip}}_{NN}$	$+4$	±2	
K	$T_1T_1 \qquad T_3T_3$	$+8J^{\mathrm{dip}}_{NN}-4J^{\mathrm{dip}}_{NNN}$	$+6.11$	0	
L	$T_1T_3 \qquad T_3T_4$	$+8J^{\mathrm{dip}}_{NN}$	$+8$	0	

of the C and A transitions are shown as dashed gray lines. The C transition, with $T_3T_2 \quad T_2^{\perp}T_3$, does not change the dipolar energy of the spin configuration, but—due to $|M_i^{\perp}| = 4$—is subject to strong chiral barrier splitting, which significantly enhances its probability compared to the mean-field barrier model at the same value of a. Typically, several T_1 strings grow during the initial demagnetization phase, and as such string separation events can lead to a sizable prevalence of $T_2^{\perp}$ vertices, which is also indicated by the cyan-shaded areas in Figs. 3(d)–3(f) and the larger number of breaks in T_1 strings within the corresponding snapshots.

B. Generalized results

The kMC simulation results presented above have been obtained for specific values of the lattice periodicity a and temperature T, while keeping the single-island magnetic moment m and switching barrier E_{sb} fixed. Variation of any of these parameters strongly affect the switching rates calculated from Eqs. (5) and (7), and, in turn, lead to vastly modified relaxation pathways. A direct comparison of simulation outcomes that differ in more than one parameter therefore requires the consideration of reduced energy or temperature scales:

Using the ratio $T_N/T \propto J^{\mathrm{dip}}_{NN}/T$ to denote the relative strength of interactions compared to the thermal energy, the transition probabilities are equivalent when varying the lattice periodicity a or temperature T (see Fig. 6 in the Appendix), as J^{dip}_{NN}/T is the relevant factor modifying the energy barrier in the Arrhenius law.

For a series of kMC simulations with varying values of a and T (Fig. 9 in the Appendix), we furthermore find that for, a given model, and normalized energies T_N/T and $20 \quad E_{\mathrm{sb}}/(k_BT) \quad 80$ the simulation results are largely equivalent. Ratios $E_{\mathrm{sb}}/(k_BT) \geqslant 20$ are consistent with values typical for metastable or slowly fluctuating nanomagnets imaged in x-ray photoelectron emission (PEEM) or magnetic force microscopy (MFM) experiments [5–8,11,12,15,16,38].

In general, the mean-field and the split-barrier models exhibit distinct relaxation behavior, as discussed above, except when approaching the paramagnetic regime with $T \quad T_N$ where the relative influence of the chiral barrier splitting on the relaxation rates vanishes [46].

C. Emergence of domain morphologies

The favored transitions A to D discussed above remain remarkably similar within the first three quantiles of relaxation, i.e., as $M^{[11]}$ decreases from 100% to 25% (which is typically achieved within a relatively small number of individual transitions). As T_3 pairs are created and T_1 strings grow, two distinct domain morphologies might emerge, which are *diagonal stripe domains* and *coral domains* (see 25% snapshots in Fig. 3).

Stripe domains are predominant for the mean-field model with strong interactions [e.g., Figs. 3(a) and 3(b)]. As T_1 strings can form independently, the relative position of the lines can match to form extended areas of T_1 tiling. Alternatively, if T_1 strings are separated by a single diagonal of T_2 vertices, then this boundary cannot be removed from the system without the generation of high-energy T_4 vertices. This very stable configuration (in addition to the limited simulation steps) makes domain consolidation—that is, domain merging and annihilation—toward a global ground state difficult and leads to a stagnation of relaxation at final magnetization values around $M^{[11]} \approx 10$–20% [Figs. 3(a) and 3(b)].

Coral domain mainly appear for an interaction regime where demagnetization is neither dominated by string propagation nor by random creation of T_3 pairs, i.e., at intermediate values for $p_{B/A}$ [dotted black line in Figs. 4(e) and 4(f)], and where a sizable fraction of $T_2^{\perp}$ are possible within the initial demagnetization [see $p_{C/A}$, gray dashed line in Figs. 4(e) and 4(f)]. The formation of coral-shaped domains can thus be directly linked to the emergence of $T_2^{\perp}$ from "charge separation" events within the propagation of T_1 strings via transitions of type C [38]. As discussed above, transitions of type C are promoted within the chiral-split barrier model, without need to invoke site-specific disorder. Therefore, the experimental observation of coral-shaped domains indicates the

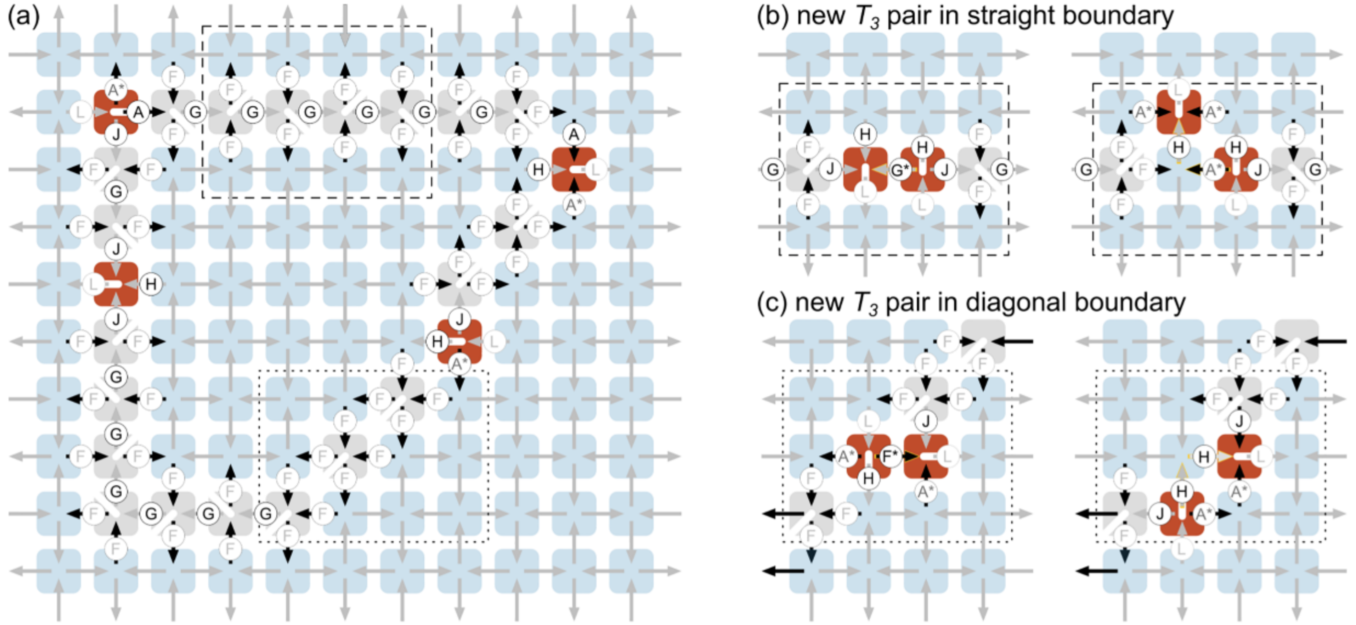

FIG. 5. Transitions at domain boundaries. Black arrows denote moments within local environments with $M_i^{\perp} \neq 0$ that enable chiral barrier splitting, and thus can lead to enhanced transition rates. Gray arrows conversely indicate environments with $M_i^{\perp} = 0$. Distinct transitions at the domain boundary are labeled, with gray labels indicating those with a high energy barrier and thus low probability. Transitions on any unlabeled spin are high-energy excitation $T_1T_1 \quad T_3T_3$ of the ground-state background which are unlikely to occur (transition type K in Table I). (a) Prototypical domain boundary separating degenerate ground states. The boundary carries a net magnetization (indicated with white lines) that follows the outline of the domain. Most switching activity will involve T_3 defects located within the boundary. [(b) and (c)] Following the creation of T_3 pairs in (b) straight and (c) diagonal domain boundaries, transition rates feature an asymmetry with respect to both ground-state domains on either side of the boundary, driving the deformation and shrinking of domains.

effect of chiral barrier splitting, in addition to the influence of lithographic defects to which these morphologies are typically attributed [21,22,38,43].

D. Relaxation at domain boundaries

As shown in Fig. 3, on a macroscopic scale, relaxation slows considerably for $M^{[11]} \quad 25\%$, indicating that the relevant switching environments and relaxation pathways effectively change, now being largely constrained to domain boundaries only. At the same time, especially in the case of the chiral-split barrier model or weak interactions, a sizable number of T_3 vertices arise with a peak around $M_{[11]} \approx 10\%$, emphasizing the vital role of high-energy vertices in the final relaxation steps to the ground state.

The cyan- and blue-shaded areas in Figs. 3(a) and 3(d) representing the population of $T_2^{\perp}$ and $T_2^{[\bar{1}\bar{1}]}$ vertices (magnetized opposite to the initial magnetization) furthermore indicate a specific sequence for the final relaxation to the ground state by the creation of extended T_1 domains and their removal via mobile T_3 vertices (red area): The emergence of $T_2^{\perp}$ vertices not only relates to the emergence of protodomains but also predates the onset of a sizable population of $T_2^{[\bar{1}\bar{1}]}$ vertices. The onset of a $T_2^{[\bar{1}\bar{1}]}$ vertex population also coincides roughly with the maximum of the T_3 population (red area), as their motion and annihilation are crucial for the consolidation of the ground-state domains. Together with the original $T_2^{[11]}$ vertices, a large fraction of these emerging $T_2^{\perp}$ and $T_2^{[\bar{1}\bar{1}]}$ vertices compound domain boundaries.

We now consider a prototypical coral domain boundary as shown in Fig. 5(a). This boundary consists mostly of T_2 vertices as well as T_3 pairs [15,40], with a straight or zigzag magnetization following the domain outline (indicated by white lines) [43]. Different transitions, depending on the local spin configuration, are marked with letters in Fig. 5 and moments for which $M_i^{\perp} \neq 0$, i.e., with transitions boosted by barrier splitting in the CB model, are marked with black arrows (see Table I for values of $E^{\mathrm{dip}}_{i \quad f}$ and $M_i^{\perp}$).

Excitations of the ground state, i.e., $T_1T_1 \quad T_3T_3$ (transition K in Table I), are energetically costly. Therefore, within the last stages of relaxation, the switching events are largely localized to the domain boundaries, further contributing to the slowdown of dynamics in the final stage of relaxation (as shown in Fig. 3). Many potential spin flips at the boundary furthermore involve a large barrier energy (labeled in light gray in Fig. 5), especially in the case for diagonal domain boundaries, as many of these promote the creation or motion of T_3 vertices. Even when considering chiral effects, many transitions remain energetically unfavorable (black arrows denote those environments that experience torque exerted by neighboring spins).

For *straight* boundaries, Fig. 5(b), the creation of a T_3 pair leads to an asymmetry with respect to the two different ground-state domains on either side of the boundary. Transition L would create a T_4 vertex and thus is kinetically suppressed, whereas transitions J and H with $E^{\mathrm{dip}}_{i \quad f} = 0$ support a high mobility of the T_3 defects to move within the boundary line or deform the domain.

For *diagonal* domain boundaries, Fig. 5(c), the presence of T_3 vertices inevitably comes hand in hand with domain deformation. Similarly to the straight boundary, a clear asymmetry in transitions contributes to the preferential shrinking of one ground-state domain over the other. Note that A* transitions are unlikely to occur within a mean-field model but can be promoted via chiral-barrier splitting in the limit of strong interactions (i.e., small lattice periodicities a).

Within our kMC simulations, we rarely reached full ground-state ordering within n^3 simulation steps due to a high fraction of random transitions (for weaker interactions) or limiting relaxation pathways. The latter is especially the case for the mean-field model with strong interactions, where size-dependent periodic boundary conditions may further reduce chances of full demagnetization. The many spin flips necessary to reach the ground state might explain the prevalence of coral-shaped domains observed in experiments where spin configurations are frozen after field-driven or thermal annealing.

V. DISCUSSION

In this work, we demonstrated how the overall relaxation towards the energetically favorable ground state can be modified profoundly by explicitly taking modifications from local torques to kinetic energy barriers into account. Although the main relaxation (i.e., reduction of the net magnetization from 100% to 25%) involves a small number of relevant transitions only, a subtle shift in their relative probability results in different emergent mesoscopic features, ranging from stringlike avalanches to coral-shaped domains in a perfect system. As our model considers intrinsic effects only in an otherwise idealized homogeneous s-ASI, the emergence of diverse domain structures implies a complementary viewpoint on effects typically attributed to extrinsic disorder by assuming a site-specific variation in the value of E_{sb}, often around 5% [21,22,38,43].

Common experimental techniques used to measure and image artificial spin systems do not have the temporal and spatial resolution to directly track the preferred rotation direction of switching nanomagnets. Hence, we have to consider indirect measures on how the chiral-split barrier model will produce better predictions for experimental systems when compared to the mean-field model, especially when considering additional randomizing effects due to extrinsic disorder.

We briefly discuss several experimental observations that could indicate an influence of kinetics affected by spin flips with favorable switching chirality.

First, the ratios between the transition rates A, B, and C determine the average length of T_1 strings, as well as the initial rate of demagnetization; however, these changes are subtle and difficult to disentangle from the effects of extrinsic disorder or temperature.

Second, the increased back-flip probability for T_3 pairs could show up in experiments as an unusual persistence of the ferromagnetic state [24].

Third, experimental results often indicate an arrested state around 20% of the final magnetization [28,32,38], at which the relaxation dynamics slow down rapidly. Inspecting domain morphologies and vertex populations (in particular T_3, $T_2^{\perp}$, and $T_2^{[\overline{11}]}$), as well as site-specific blocking temperatures [64–66], could indicate the relative importance of the different relaxation pathways leading to these states (without ascertaining whether they originate from disorder or chiral-split barriers).

Fourth, and finally, quantifying the switching activity at boundaries between ground-state domains [15,34,40,43] might give crucial insights to favored transitions and how they relate to local disorder compared to the effect of barrier reductions due to local torques.

VI. CONCLUSIONS

In conclusion, in this work we consider the effect of different models based on a point-dipole description of switching barriers in s-ASI, and follow the evolution of a perfect system using kinetic Monte Carlo simulations. We find relaxation dominated by avalanches of T_1 strings in the limit of the (static energy-only) mean-field barrier model, contrasted with the emergence of more complex coral-shaped domains by taking into account the effect of local torques that lead to favored chiral switching pathways. We find differences between the models in particular with respect to their influence on initial demagnetization, the role of $T_2^{\perp}$ vertices in the formation of initial domains, and relaxation pathways at domain boundaries.

Furthermore, we find that analyzing single vertex populations, typically T_3 in literature, is not as informative as considering also the sizable fraction $T_2^{\perp}$ and $T_2^{[\overline{11}]}$ vertices. These vertex distributions develop concomitantly, and thus give insight into the relative importance of different relaxation pathways.

Our results make a step towards creating more realistic, but still highly simplified, models to describe the switching in experimental artificial spin systems dominated by coherent reversal modes and strong pairwise interactions. Although we here focus on the s-ASI with periodic boundary conditions, where each moment has the same environment, the effect of the local torques would be even more pronounced in the case of artificial spin systems with mixed-vertex coordination and different boundary conditions [65,67–70].

Descriptive models that capture the relevant features of transition kinetics are key for successful simulations of the evolution of large arrays, which are otherwise too costly or plainly unrealistic to simulate with micromagnetic approaches. Simulation tools based on simplified but physically realistic descriptions [43,44] therefore make it possible to successfully model the evolution of extended spin ices [71] or develop sample geometries tailored to specific nanomagnetic logic or unconventional computing applications [11,12,72,73].

ACKNOWLEDGMENTS

M.M. and P.V. acknowledge support from the Spanish Ministry of Science, Innovation and Universities under the Maria de Maeztu Units of Excellence Programme (Grant No. CEX2020-001038-M) and the predoctoral Grant No. PRE2019-088070 (M.M.), as well as from the Spanish Ministry of Science and Innovation and the European Union

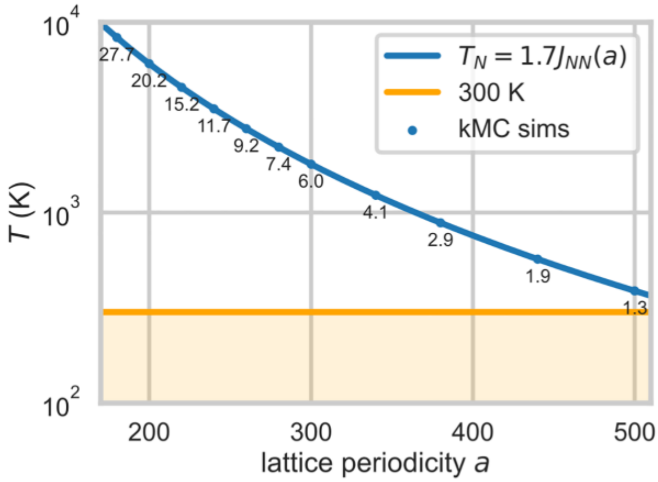

FIG. 6. Néel temperature in dependence of lattice periodicity a. Points indicate values of a for which kMC simulations were performed with numbers underneath indicating the ratio T_N/T, i.e., how far within the ordered phase the demagnetization was simulated.

under Project No. PID2021-123943NB-I00 (OPTOMETAMAG). N.L. received funding from the European Research Council (ERC) under European Union's Horizon 2020 research and innovation program under the Marie Sklodowska Curie Grant Agreement No. 844304 (LICONAMCO), as well as support by a UKRI Future Leader Fellowship Grant No. MR/X033910/1 (LIONESS).

DATA AVAILABILITY

The data that support the findings of this article are openly available [74].

APPENDIX

1. Thermal regimes

Figure 6 shows the critical Néel temperature $T_N(a) = 1.7J_{NN}^{\mathrm{dip}}$ in dependence of lattice periodicity a, calculated using Eq. (1), in comparison to the simulation temperature $T = 300\,\mathrm{K}$. As indiciated by the annotated ratio T_N/T, the demagnetization simulations (run at lattice periodicities a marked by blue dots) span a thermal regime from just below T_N to deep within the ordered phase.

2. Finite-size effects

Figure 7 investigates the possible adverse effects of finite size and periodic boundary conditions on the simulation results, by comparing the demagnetization at system sizes of $n = 20$, 30, 50, and 80. The results for $n = 20$ are strongly affected by finite-size effects as T_1 strings propagate rapidly, wrap the system, and then interfere with their starting points. Results for $n \geqslant 30$ do closely resemble each other. For the main discussion, we chose $n = 50$ as a compromise between good statistics and computational resources, and $n = 30$ for the phase diagrams shown in Fig. 9.

3. Larger lattice periodicities

Figure 8 shows complementary simultations performed for lattice periodicities of $a = 300$, 340, and 380 nm. With increasing lattice periodicity a, the interaction energy J_{NN}^{dip} decreases (or, conversely, T_N approaches the simulation temperature T). In this case, the effect of barrier splitting becomes less pronounced, leading to converging behavior between the mean-field and split-barrier model. Nevertheless, there a slight difference for T_3 vertex popoulation (red area) of the chiral-split barrier in the late phase of demagnetization remains, as indicated by a small bump around $M^{[11]} \approx 10\%$, which is linked to relaxation processes localized at domain boundaries.

4. Generalized phase diagram

In addition to the choice of mean-field vs split-barrier model, the square-ice relaxation behavior is determined by the balance of two system-dependent energy contributions with the thermal energy k_BT providing a scale for comparison. Figure 9 compares kMC simulations at different lattice constants a (170 to 500 nm) and temperatures T (200 K to 800 K) at a system size of $n = 30$ (20 averages each). All other parameters, i.e., m and E_{sb}, remain as described under Methods.

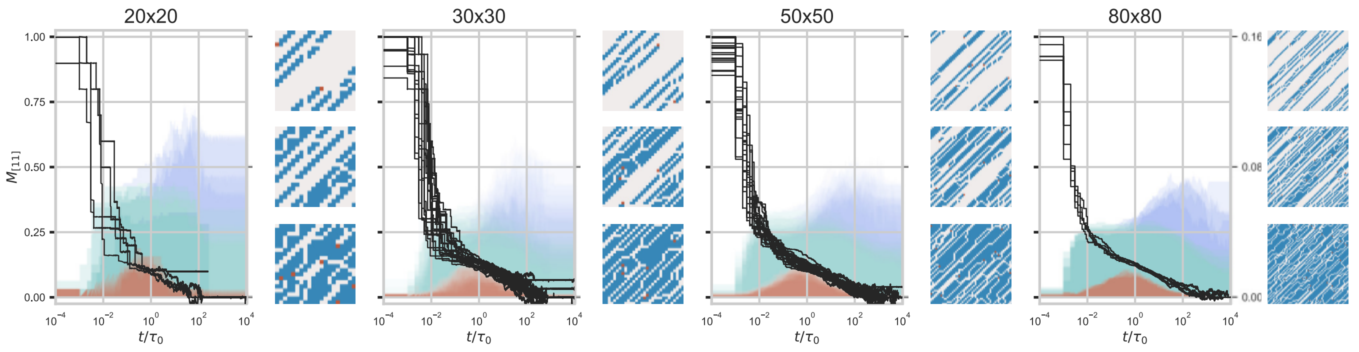

FIG. 7. kMC simulations for the split-barrier model in dependence of system size for fixed $a = 260\,\mathrm{nm}$ and $T = 300\,\mathrm{K}$ and $n \times n$ vertices with $n = (20, 30, 50, 80)$ comparing the results of (5,20,20,5) kMC simulation runs, respectively. All other simulations settings are unchanged. Equivalently to Fig. 3, the four panels compare the time dependence of demagnetization (black lines), T_3 vertex population (red), as well as $T_2^{\perp}$ (cyan, from zero) and $T_2^{[\bar{1}\bar{1}]}$ (blue). Insets on the right show representative spatial configurations of vertices at times where the net magnetization is at 75%, 50% and 25% of its initial value.

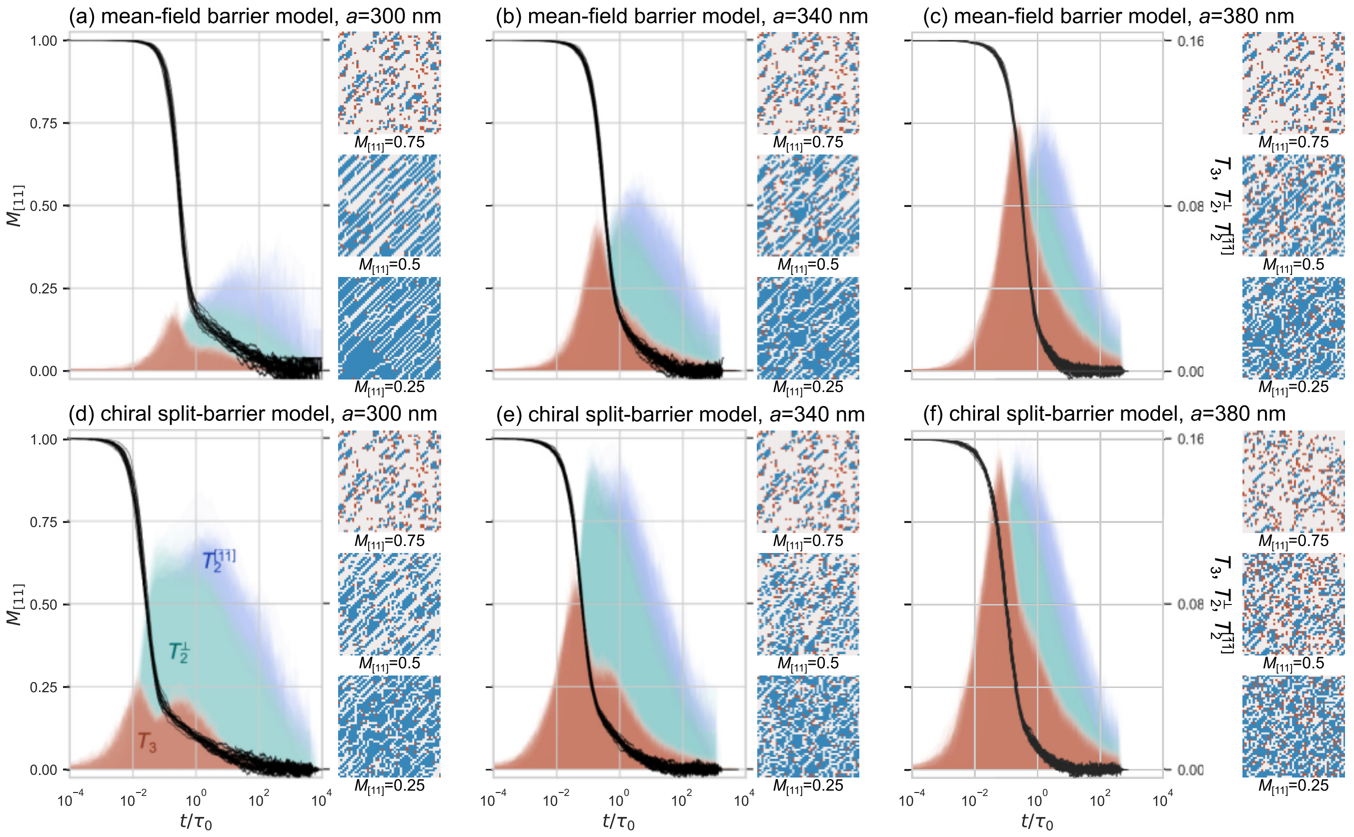

FIG. 8. Demagnetization behavior for lattice periodicities a above 300 nm for [(a)–(c)] the mean-field barrier model and [(d)–(f)] the chiral-split barrier model. Legend and annotations are equivalent to Fig. 3.

The first energy scale is given by the ratio between the single-particle barrier and thermal energy, $E_{\mathrm{sb}}/(k_BT)$, which denotes the thermal stability of an isolated magnetic nanoisland. For the simulations discussed in the main manuscript, with $E_{\mathrm{sb}} = 1.327$ eV and $T = 300$ K this ratio is ≈51, hence switching events are generally rare. As shown in Fig. 9, the plotted characteristics are largely invariant on the choice of 20 $E_{\mathrm{sb}}/(k_BT)$ 60, and the effect of chiral barrier splitting, when compared to the mean-field model, is pronounced, as predicted in Ref. [46] for large ratios of $E_{\mathrm{sb}}/(k_BT)$. Such values of $E_{\mathrm{sb}}/(k_BT)$ are consistent with many of the experimental studies that we cited in our work, relying on imaging of thermally stable nanomagnets via PEEM or MFM methods.

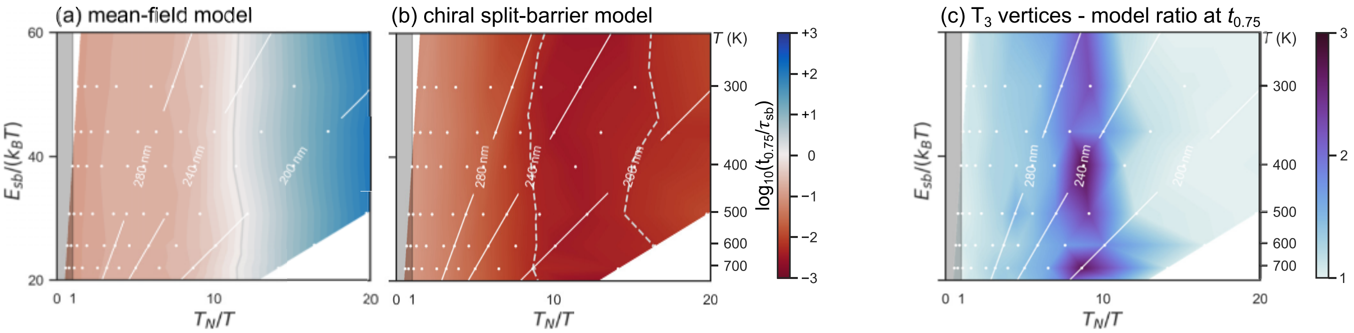

FIG. 9. Generalized phase diagram. To allow for a general comparison, values are plotted for each simulation (white points) in dependence of the relative single-particle barrier $E_{\mathrm{sb}}/(k_BT)$ [corresponding values of T are shown on the right scale of (b)] and relative interaction temperature T_N/T [values of constant $a = 200$ nm, 240 nm and 280 nm are marked with white lines, the paramagnetic region is shaded in gray]. [(a) and (b)] Demagnetization time $t_{0.75} = t(M^{[11]} = 75\%)$ divided by τ_{sb} for the (a) mean-field and (b) split-barrier model [comparable to Fig. 2]. (a) For the mean-field model and T_N/T 11 the relaxation shows a slow down (gray line, blue region) even beyond the speed of single-particle relaxation due to correlated string propagation. (b) For the split-barrier model and T_N/T 16 the initial demagnetization is delayed due to rapid creation-annihilation events of T_3 pairs (dashed lines). (c) Ratio of the number of T_3 vertices at $t_{0.75}$ between the split-barrier and mean-field barrier model. For values $T_N/T \approx 9$, two to three times more T_3 vertices are created for the split-barrier, coinciding with an enhancement of string separation events via the formation of $T_2^{\perp}$ vertices, leading to complex domain structures.

The second energy scale is given by the interaction strength $J_{NN}^{\mathrm{dip}}(a)/T$, respectively the Néel temperature $T_N(a) = 1.7J_{NN}^{\mathrm{dip}}$ [42,62]. The models resemble each other for $T \quad T_N$, as the influence of chiral-barrier splitting disappears in the limit of superparamagnetic fluctuations. Conversely, at $T \quad 0$ (respectively, high values of T_N/T) the effect of barrier-splitting becomes more pronounced (including the occurrence of kinetic blocking of demagnetization due to rapid and subsequent T_3 creation-annihilation events).

[1] R. F. Wang, C. Nisoli, R. S. Freitas, J. Li, W. McConville, B. J. Cooley, M. S. Lund, N. Samarth, C. Leighton, V. H. Crespi, and P. Schiffer, Artificial spin ice in a geometrically frustrated lattice of nanoscale ferromagnetic islands, Nature (London) **439**, 303 (2006).

[2] C. Nisoli, R. Moessner, and P. Schiffer, *Colloquium*: Artificial spin ice: Designing and imaging magnetic frustration, Rev. Mod. Phys. **85**, 1473 (2013).

[3] L. Heyderman and R. Stamps, Artificial ferroic systems: Novel functionality from structure, interactions and dynamics, J. Phys.: Condens. Matter **25**, 363201 (2013).

[4] S. H. Skjaervø, C. H. Marrows, R. L. Stamps, and L. J. Heyderman, Advances in artificial spin ice, Nat. Rev. Phys. **2**, 13 (2019).

[5] E. Mengotti, L. J. Heyderman, A. F. Rodriguez, A. Bisig, L. L. Guyader, F. Nolting, and H. B. Braun, Building blocks of an artificial kagome spin ice: Photoemission electron microscopy of arrays of ferromagnetic islands, Phys. Rev. B **78**, 144402 (2008).

[6] E. Mengotti, L. J. Heyderman, A. F. Rodriguez, F. Nolting, R. V. Hugli, and H.-B. Braun, Real-space observation of emergent magnetic monopoles and associated Dirac strings in artificial kagome spin ice, Nat. Phys. **7**, 68 (2011).

[7] W. R. Branford, S. Ladak, D. E. Read, K. Zeissler, and L. F. Cohen, Emerging chirality in artificial spin ice, Science **335**, 1597 (2012).

[8] B. Canals, I.-A. Chioar, V.-D. Nguyen, M. Hehn, D. Lacour, F. Montaigne, A. Locatelli, T. O. Mentes, B. S. Burgos, and N. Rougemaille, Fragmentation of magnetism in artificial kagome dipolar spin ice, Nat. Commun. **7**, 11446 (2016).

[9] O. Sendetskyi, L. Anghinolfi, V. Scagnoli, G. Möller, N. Leo, A. Alberca, J. Kohlbrecher, J. Lüning, U. Staub, and L. J. Heyderman, Magnetic diffuse scattering in artificial kagome spin ice, Phys. Rev. B **93**, 224413 (2016).

[10] A. Imre, G. Csaba, L. Ji, A. Orlov, G. H. Bernstein, and W. Porod, Majority logic gate for magnetic quantum-dot cellular automata, Science **311**, 205 (2006).

[11] H. Arava, P. M. Derlet, J. Vijayakumar, J. Cui, N. S. Bingham, A. Kleibert, and L. J. Heyderman, Computational logic with square rings of nanomagnets, Nanotechnol. **29**, 265205 (2018).

[12] H. Arava, N. Leo, D. Schildknecht, J. Cui, J. Vijayakumar, P. M. Derlet, A. Kleibert, and L. J. Heyderman, Engineering relaxation pathways in building blocks of artificial spin ice for computation, Phys. Rev. Appl. **11**, 054086 (2019).

[13] F. Caravelli and C. Nisoli, Logical gates embedding in artificial spin ice, New J. Phys. **22**, 103052 (2020).

[14] J. C. Gartside, K. D. Stenning, A. Vanstone, H. H. Holder, D. M. Arroo, T. Dion, F. Caravelli, H. Kurebayashi, and W. R. Branford, Reconfigurable training and reservoir computing in an artificial spin-vortex ice via spin-wave fingerprinting, Nat. Nanotechnol. **17**, 460 (2022).

[15] J. P. Morgan, A. Stein, S. Langridge, and C. H. Marrows, Thermal ground-state ordering and elementary excitations in artificial magnetic square ice, Nat. Phys. **7**, 75 (2011).

[16] J. Lehmann, A. Bortis, P. M. Derlet, C. Donnelly, N. Leo, L. J. Heyderman, and M. Fiebig, Relation between microscopic interactions and macroscopic properties in ferroics, Nat. Nanotechnol. **15**, 896 (2020).

[17] V. Kapaklis, U. B. Arnalds, A. Harman-Clarke, E. T. Papaioannou, M. Karimipour, P. Korelis, A. Taroni, P. C. W. Holdsworth, S. T. Bramwell, and B. Hjörvarsson, Melting artificial spin ice, New J. Phys. **14**, 035009 (2012).

[18] A. Farhan, P. M. Derlet, A. Kleibert, A. Balan, R. V. Chopdekar, M. Wyss, L. Anghinolfi, F. Nolting, and L. J. Heyderman, Exploring hyper-cubic energy landscapes in thermally active finite artificial spin-ice systems, Nat. Phys. **9**, 375 (2013).

[19] V. Kapaklis, U. B. Arnalds, A. Farhan, R. V. Chopdekar, A. Balan, A. Scholl, L. J. Heyderman, and B. Hjorvarsson, Thermal fluctuations in artificial spin ice, Nat. Nanotechnol. **9**, 514 (2014).

[20] R. F. Wang, J. Li, W. McConville, C. Nisoli, X. Ke, J. W. Freeland, V. Rose, M. Grimsditch, P. Lammert, V. H. Crespi, and P. Schiffer, Demagnetization protocols for frustrated interacting nanomagnet arrays, J. Appl. Phys. **101**, 09J104 (2007).

[21] Z. Budrikis, *Disorder, Edge, and Field Protocol Effects in Athermal Dynamics of Artificial Spin Ice* (Academic Press, San Diego, CA, 2014), p. 109.

[22] I. Gilbert, G.-W. Chern, B. Fore, Y. Lao, S. Zhang, C. Nisoli, and P. Schiffer, Direct visualization of memory effects in artificial spin ice, Phys. Rev. B **92**, 104417 (2015).

[23] N. S. Bingham, S. Rooke, J. Park, A. Simon, W. Zhu, X. Zhang, J. Batley, J. D. Watts, C. Leighton, K. A. Dahmen, and P. Schiffer, Experimental realization of the 1D random field Ising model, Phys. Rev. Lett. **127**, 207203 (2021).

[24] N. S. Bingham, X. Zhang, J. Ramberger, O. Heinonen, C. Leighton, and P. Schiffer, Collective ferromagnetism of artificial square spin ice, Phys. Rev. Lett. **129**, 067201 (2022).

[25] C. Nisoli, On thermalization of magnetic nano-arrays at fabrication, New J. Phys. **14**, 035017 (2012).

[26] D. Levis, L. F. Cugliandolo, L. Foini, and M. Tarzia, Thermal phase transitions in artificial spin ice, Phys. Rev. Lett. **110**, 207206 (2013).

[27] J. P. Morgan, J. Akerman, A. Stein, C. Phatak, R. M. L. Evans, S. Langridge, and C. H. Marrows, Real and effective thermal equilibrium in artificial square spin ices, Phys. Rev. B **87**, 024405 (2013).

[28] J. M. Porro, A. Bedoya-Pinto, A. Berger, and P. Vavassori, Exploring thermally induced states in square artificial spin-ice arrays, New J. Phys. **15**, 055012 (2013).

[29] S. Zhang, I. Gilbert, C. Nisoli, G.-W. Chern, M. J. Erickson, L. O'Brien, C. Leighton, P. E. Lammert, V. H. Crespi, and P. Schiffer, Crystallites of magnetic charges in artificial spin ice, Nature (London) **500**, 553 (2013).

[30] X. Zhang, Y. Lao, J. Sklenar, N. S. Bingham, J. T. Batley, J. D. Watts, C. Nisoli, C. Leighton, and P. Schiffer, Understanding thermal annealing of artificial spin ice, APL Mater. **7**, 111112 (2019).

[31] M. S. Andersson, S. D. Pappas, H. Stopfel, E. Östman, A. Stein, P. Nordblad, R. Mathieu, B. Hjörvarsson, and V. Kapaklis, Thermally induced magnetic relaxation in square artificial spin ice, Sci. Rep. **6**, 37097 (2016).

[32] S. A. Morley, D. Alba Venero, J. M. Porro, S. T. Riley, A. Stein, P. Steadman, R. L. Stamps, S. Langridge, and C. H. Marrows, Vogel-Fulcher-Tammann freezing of a thermally fluctuating artificial spin ice probed by x-ray photon correlation spectroscopy, Phys. Rev. B **95**, 104422 (2017).

[33] O. Sendetskyi, V. Scagnoli, N. Leo, L. Anghinolfi, A. Alberca, J. Lüning, U. Staub, P. M. Derlet, and L. J. Heyderman, Continuous magnetic phase transition in artificial square ice, Phys. Rev. B **99**, 214430 (2019).

[34] X. M. Chen, B. Farmer, J. S. Woods, S. Dhuey, W. Hu, C. Mazzoli, S. B. Wilkins, R. V. Chopdekar, A. Scholl, I. K. Robinson, L. E. De Long, S. Roy, and J. T. Hastings, Spontaneous magnetic superdomain wall fluctuations in an artificial antiferromagnet, Phys. Rev. Lett. **123**, 197202 (2019).

[35] H. Arava, E. Y. Vedmedenko, J. Cui, J. Vijayakumar, A. Kleibert, and L. J. Heyderman, Control of emergent magnetic monopole currents in artificial spin ice, Phys. Rev. B **102**, 144413 (2020).

[36] M. Goryca, X. Zhang, J. Li, A. L. Balk, J. D. Watts, C. Leighton, C. Nisoli, P. Schiffer, and S. A. Crooker, Field-induced magnetic monopole plasma in artificial spin ice, Phys. Rev. X **11**, 011042 (2021).

[37] M. Goryca, X. Zhang, J. D. Watts, C. Nisoli, C. Leighton, P. Schiffer, and S. A. Crooker, Magnetic field dependent thermodynamic properties of square and quadrupolar artificial spin ice, Phys. Rev. B **105**, 094406 (2022).

[38] A. Farhan, P. M. Derlet, A. Kleibert, A. Balan, R. V. Chopdekar, M. Wyss, J. Perron, A. Scholl, F. Nolting, and L. J. Heyderman, Direct observation of thermal relaxation in artificial spin ice, Phys. Rev. Lett. **111**, 057204 (2013).

[39] R. V. Hügli, G. Duff, B. O'Conchuir, E. Mengotti, A. F. Rodríguez, F. Nolting, L. J. Heyderman, and H. B. Braun, Artificial kagome spin ice: Dimensional reduction, avalanche control and emergent magnetic monopoles, Philos. Trans. R. Soc. A **370**, 5767 (2012).

[40] Z. Budrikis, K. Livesey, J. Morgan, J. Akerman, A. Stein, S. Langridge, C. Marrows, and R. Stamps, Domain dynamics and fluctuations in artificial square ice at finite temperatures, New J. Phys. **14**, 035014 (2012).

[41] P. Jensen and G. Pastor, Dipole coupling induced magnetic ordering in an ensemble of nanostructured islands, physica status solidi (a) **189**, 527 (2002).

[42] R. C. Silva, F. S. Nascimento, L. A. S. Mól, W. A. Moura-Melo, and A. R. Pereira, Thermodynamics of elementary excitations in artificial magnetic square ice, New J. Phys. **14**, 015008 (2012).

[43] J. H. Jensen, A. Strømberg, O. R. Lykkebø, A. Penty, J. Leliaert, M. Själander, E. Folven, and G. Tufte, Flatspin: A large-scale artificial spin ice simulator, Phys. Rev. B **106**, 064408 (2022).

[44] J. Maes, D. De Gusem, I. Lateur, J. Leliaert, A. Kurenkov, and B. V. Waeyenberge, The design, verification, and applications of Hotspice: A Monte Carlo simulator for artificial spin ice, Comput. Phys. Commun. **313**, 109643 (2025).

[45] S. Koraltan, M. Pancaldi, N. Leo, C. Abert, C. Vogler, K. Hofhuis, F. Slanovc, F. Bruckner, P. Heistracher, M. Menniti, P. Vavassori, and D. Suess, Dependence of energy barrier reduction on collective excitations in square artificial spin ice: A comprehensive comparison of simulation techniques, Phys. Rev. B **102**, 064410 (2020).

[46] N. Leo, M. Pancaldi, S. Koraltan, P. V. González, C. Abert, C. Vogler, F. Slanovc, F. Bruckner, P. Heistracher, K. Hofhuis, M. Menniti, D. Suess, and P. Vavassori, Chiral switching and dynamic barrier reductions in artificial square ice, New J. Phys. **23**, 033024 (2021).

[47] C. Phatak, M. Pan, A. K. Petford-Long, S. Hong, and M. De Graef, Magnetic interactions and reversal of artificial square spin ices, New J. Phys. **14**, 075028 (2012).

[48] W. F. Brown, Thermal fluctuations of a single-domain particle, Phys. Rev. **130**, 1677 (1963).

[49] J. Langer, Statistical theory of the decay of metastable states, Ann. Phys. **54**, 258 (1969).

[50] S. Krause, G. Herzog, T. Stapelfeldt, L. Berbil-Bautista, M. Bode, E. Y. Vedmedenko, and R. Wiesendanger, Magnetization reversal of nanoscale islands: How size and shape affect the Arrhenius prefactor, Phys. Rev. Lett. **103**, 127202 (2009).

[51] M. Stier, A. Neumann, A. Philippi-Kobs, H. P. Oepen, and M. Thorwart, Implications of a temperature-dependent magnetic anisotropy for superparamagnetic switching, J. Magn. Magn. Mater. **447**, 96 (2018).

[52] L. Desplat and J.-V. Kim, Entropy-reduced retention times in magnetic memory elements: A case of the Meyer-Neldel compensation rule, Phys. Rev. Lett. **125**, 107201 (2020).

[53] S. Kanai, K. Hayakawa, H. Ohno, and S. Fukami, Theory of relaxation time of stochastic nanomagnets, Phys. Rev. B **103**, 094423 (2021).

[54] J. A. Osborn, Demagnetizing factors of the general ellipsoid, Phys. Rev. **67**, 351 (1945).

[55] D. X. Chen, J. A. Brug, and R. B. Goldfarb, Demagnetizing factors for cylinders, IEEE Trans. Magn. **27**, 3601 (1991).

[56] R. Cowburn, Property variation with shape in magnetic nanoelements, J. Phys. D **33**, R1 (2000).

[57] A. Bortz, M. Kalos, and J. Lebowitz, A new algorithm for Monte Carlo simulation of Ising spin systems, J. Comput. Phys. **17**, 10 (1975).

[58] K. A. Fichthorn and W. H. Weinberg, Theoretical foundations of dynamical Monte Carlo simulations, J. Chem. Phys. **95**, 1090 (1991).

[59] M. Newman and G. Barkema, *Monte Carlo Methods in Statistical Physics* (Oxford University Press, New York, 1999), Vol. 24.

[60] M. Pancaldi, Kinetic Monte Carlo simulations for square ASI systems (2020), https://github.com/matteopanca/kmc_asi.

[61] M. Pancaldi, Study of geometrical frustration and thermal activation in arrays of magnetic nanostructures, Ph.D. thesis, Universidad del País Vasco UPV/EHU, Bilbao, 2018.

[62] G. Möller and R. Moessner, Artificial square ice and related dipolar nanoarrays, Phys. Rev. Lett. **96**, 237202 (2006).

[63] J. Morgan, A. Stein, S. Langridge, and C. Marrows, Magnetic reversal of an artificial square ice: Dipolar correlation and charge ordering, New J. Phys. **13**, 105002 (2011).

[64] J. Li, S. Zhang, J. Bartell, C. Nisoli, X. Ke, P. E. Lammert, V. H. Crespi, and P. Schiffer, Comparing frustrated and unfrustrated clusters of single-domain ferromagnetic islands, Phys. Rev. B **82**, 134407 (2010).

[65] I. Gilbert, Y. Lao, I. Carrasquillo, L. O'Brien, J. D. Watts, M. Manno, C. Leighton, A. Scholl, C. Nisoli, and P. Schiffer, Emergent reduced dimensionality by vertex frustration in artificial spin ice, Nat. Phys. **12**, 162 (2016).

[66] N. Keswani, R. Singh, Y. Nakajima, T. Som, and P. Das, Accessing low-energy magnetic microstates in square artificial spin ice vertices of broken symmetry in static magnetic field, Phys. Rev. B **102**, 224436 (2020).

[67] M. J. Morrison, T. R. Nelson, and C. Nisoli, Unhappy vertices in artificial spin ice: New degeneracies from vertex frustration, New J. Phys. **15**, 045009 (2013).

[68] I. Gilbert, G.-W. Chern, S. Zhang, L. O'Brien, B. Fore, C. Nisoli, and P. Schiffer, Emergent ice rule and magnetic charge screening from vertex frustration in artificial spin ice, Nat. Phys. **10**, 670 (2014).

[69] Y. Lao, F. Caravelli, M. Sheikh, J. Sklenar, D. Gardeazabal, J. D. Watts, A. M. Albrecht, A. Scholl, K. Dahmen, C. Nisoli, and P. Schiffer, Classical topological order in the kinetics of artificial spin ice, Nat. Phys. **14**, 723 (2018).

[70] H. Saglam, A. Duzgun, A. Kargioti, N. Harle, X. Zhang, N. S. Bingham, Y. Lao, I. Gilbert, J. Sklenar, J. D. Watts, J. Ramberger, D. Bromley, R. V. Chopdekar, L. O'Brien, C. Leighton, C. Nisoli, and P. Schiffer, Entropy-driven order in an array of nanomagnets, Nat. Phys. **18**, 706 (2022).

[71] J. H. Jensen, A. Strømberg, I. Breivik, A. Penty, M. A. Niño, M. W. Khaliq, M. Foerster, G. Tufte, and E. Folven, Clocked dynamics in artificial spin ice, Nat. Commun. **15**, 964 (2024).

[72] D. A. Allwood, M. O. A. Ellis, D. Griffin, T. J. Hayward, L. Manneschi, M. F. K. H. Musameh, S. O'Keefe, S. Stepney, C. Swindells, M. A. Trefzer, E. Vasilaki, G. Venkat, I. Vidamour, and C. Wringe, A perspective on physical reservoir computing with nanomagnetic devices, Appl. Phys. Lett. **122**, 040501 (2023).

[73] R. L. Stamps, R. B. Popy, and J. van Lierop, Active inference demonstrated with artificial spin ice, arXiv:2401.12211.

[74] N. Leo, Relaxation pathways and emergence of domains in square artificial spin ice, https://zenodo.org/records/15548088.